Title

Geomechanical simulation of the stress tensor rotation caused by injection of cold water in a deep geothermal reservoir

Journal

Journal of Geophysical Research: Solid Earth, 120(12)

ISSN

2169-9313

Authors

Jeanne, Pierre
Rutqvist, Jonny
Dobson, Patrick F
et al.

Publication Date

2015-12-01

DOI

10.1002/2015jb012414

Peer reviewed

AGU PUBLICATIONS

JGR

Journal of Geophysical Research: Solid Earth

RESEARCH ARTICLE
10.1002/2015JB012414

Key Points:
- Changes in stress tensor orientation are caused by thermal processes
- Development of a complex stress state distribution around the cooling area
- This rotation favors the microseismicity deep below the injection wells

Correspondence to:
P. Jeanne,
pjeanne@lbl.gov

Citation:
Jeanne, P., J. Rutqvist, P. F. Dobson, J. Garcia, M. Walters, C. Hartline, and A. Borgia (2015), Geomechanical simulation of the stress tensor rotation caused by injection of cold water in a deep geothermal reservoir, *J. Geophys. Res. Solid Earth*, *120*, doi:10.1002/2015JB012414.

Received 31 JUL 2015
Accepted 2 NOV 2015
Accepted article online 12 NOV 2015

Geomechanical simulation of the stress tensor rotation caused by injection of cold water in a deep geothermal reservoir

Pierre Jeanne[1], Jonny Rutqvist[1], Patrick F. Dobson[1], Julio Garcia[2], Mark Walters[2], Craig Hartline[2], and Andrea Borgia[1]

[1]Energy Geoscience Division, Lawrence Berkeley National Laboratory, Berkeley, California, USA, [2]Calpine Corporation, Middletown, California, USA

Abstract We present a three-dimensional thermohydromechanical numerical study of the evolution and distribution of the stress tensor within the northwest part of The Geysers geothermal reservoir (in California), including a detailed study of the region around one injection well from 2003 to 2012. Initially, after imposing a normal faulting stress regime, we calculated local changes in the stress regime around injection wells. Our results were compared with previously published studies in which the stress state was inferred from inverting the focal plane mechanism of seismic events. Our main finding is that changes in stress tensor orientation are caused by injection-induced progressive cooling of the reservoir, as well as by the seasonal variations in injection rate. Because of the gravity flow and cooling around a liquid zone formed by the injection, the vertical stress reduction is larger and propagates far below the injection well. At the same time, the horizontal stress increases, mostly because of stress redistribution below and above the cooling area. These two phenomena cause the rotation of the stress tensor and the appearance of a strike-slip regime above, inside, and below the cooling area. The cooling and the associated rotation of the stress regime can play a significant role in the observed long-term deepening of the microseismicity below active injection wells.

1. Introduction

The stimulation of geothermal reservoirs by massive injection of cold water is frequently accompanied by induced seismicity [*Davis and Frohlich*, 1993]. This induced seismicity can yield valuable information about reservoir properties and the stimulation zone (e.g., size, depth, and changes in permeability). On the other hand, there is a risk that induced seismic events could be sufficiently large to be felt by, and consequently potentially unsettle, local communities and could (in a worst-case scenario) potentially jeopardize a project (e.g., the discontinuation of an Enhanced Geothermal System (EGS) project in Basel, Switzerland [*Häring et al.*, 2008]). For these reasons, it is highly desirable to have a firm understanding of the geomechanical processes and injection-induced stress changes occurring at reservoir depth. This understanding of reservoir geomechanical processes and stress is needed to be able to characterize an EGS and its evolution, as well as to minimize the risk of felt seismic events. As a result of a growing interest in these issues, a number of scientific studies have recently been published on the spatiotemporal changes of the stress state inside geothermal reservoirs during injection of cold water [*Martínez-Garzón et al.*, 2013, 2014; *Altmann et al.*, 2014; *Boyle and Zoback*, 2014; *Schoenball et al.*, 2014].

Most of the aforementioned studies were performed at The Geysers geothermal field (California), where the presence of a dense local seismic monitoring network provides the largest existing data set of induced seismicity. Using this data, a number of studies related to the stress state have been conducted using inversion of focal plane mechanism [*Oppenheimer*, 1986; *Boyle and Zoback*, 2013; *Martínez-Garzón et al.*, 2013; *Boyle and Zoback*, 2014]. These studies all indicate that The Geysers is subject to a normal/strike-slip faulting regime ($S_V \approx S_{Hmax} > S_{hmin}$) with an average S_{Hmax} orientation ranging between N15 and N26. However, each of these studies also indicated various characteristics of a spatiotemporal stress state evolution:

1. *Oppenheimer* [1986], from the inversion of 210 fault plane solutions over the entire Geysers geothermal reservoir, found that maximum and intermediate compressive principal stresses (σ_1 and σ_2) are so nearly equal that the orientation of σ_1 and σ_2 could interchange at depths less than 1 km. *Oppenheimer* [1986] explained this phenomenon by the reduction of the lithostatic load (S_V) toward the surface.

2. *Boyle and Zoback* [2014], from focal plane mechanisms of 6147 events recorded during 2005–2012 inside the northwest part of The Geysers geothermal field, showed that the orientation of S_{Hmax} is very similar to the regional orientation of S_{Hmax}. This result suggests that neither thermal stresses nor the pressure front associated with movement of fluids and steam (caused by injection and production activities over the past 50 years) have perturbed the orientation of S_{Hmax} at the scale considered.
3. Finally, *Martínez-Garzón et al.* [2013], also inside the northwest part of The Geysers geothermal field (but at a much smaller scale than *Boyle and Zoback* [2014]) and during almost the same period (from September 2007 to June 2012), analyzed ~16,800 seismic events occurring around a single injection well (Prati-9). *Martínez-Garzón et al.* [2013] observed a normal faulting regime at the reservoir depth bounded by a strike-slip regime above and below. The causes of these changes are still not well understood. They could be caused by the poroelastic effects related to reservoir depletion, i.e., on a time scale of decades [*Segall and Fitzgerald*, 1998], or related to the different geological formations within and above/below the reservoir [*Calpine Corporation*, 2012]. *Martínez-Garzón et al.* [2013] also highlighted significant rotations in the orientation of the maximum compressive principal stress (σ_1), in response to changes in the fluid injection rates. They observed that σ_1 tilted from vertical toward the original σ_2 direction (S_{Hmax}) by approximately 20° when injection rates were at their peak level.

Even if these studies found the same general results (stress regime and S_{Hmax} orientation), they focused on different scales and locations of The Geysers (entire Geysers, a part of the Northwest Geysers, and around one injection well) where the stress regime inside the geothermal field changes with depth. These studies show the complexity involved in fully describing the spatiotemporal evolution of the stress state caused by fluid production and massive injection of cold water in a geothermal field. Here we present a three-dimensional thermohydromechanical (THM) numerical simulation to study the evolution and distribution of the stress tensor within the northwest part of The Geysers geothermal reservoir, focusing on the transient evolution around one well (Prati-9) up to 2012. In the following, we first present the study area and our numerical simulation and then compare our results with the aforementioned Geysers studies. Finally, we discuss how changes in stress tensor could impact the long-term evolution of induced seismicity around active injection wells.

2. The Northwest Geysers Area

The Geysers geothermal field is the largest geothermal electricity-generating geothermal operation in the world and has been in commercial production since 1960. It is a vapor-dominated geothermal reservoir. The main geologic units include graywacke in the normal temperature reservoir (NTR) and metamorphosed biotite hornfelsic metagraywacke (hornfels) in the high-temperature reservoir (HTR). These two geothermal reservoirs are bounded above by unfractured greywacke, which serves as a caprock, and below by young granitic intrusive rocks (felsite), which are thought to be as young as about 5000–10,000 years before present [*Williams et al.*, 1993].

Structurally, The Geysers is within the terrane of the San Andreas Fault system, which is influenced by Franciscan age subduction, Tertiary thrust faulting, and high-angle Quaternary faults [*Garcia et al.*, 2015]. It appears that only the Quaternary faults extend to reservoir depth [*Garcia et al.*, 2015]. During studies conducted in support of the Northwest Geysers EGS Demonstration Project [*Garcia et al.*, 2015], where water was injected in Prati-32 (P-32) (Figure 1a), *Jeanne et al.* [2014a, 2014b] showed that the Quaternary faults (Squaw Creek Fault) trending N130 act as a conduit and favor fluid pressure diffusion, whereas the Quaternary faults trending N050 (Caldwell Pines Fault) act as an impermeable barrier creating hydraulically separated reservoir compartments. Seismic tomography performed in this area [*Hutchings et al.*, 2014] suggests that the other Quaternary faults have similar hydraulic behavior.

Figure 1b compares the V_P distribution at −1995 m below sea level with the structural setting. The V_P distribution shows how the main reservoir is bounded by the Caldwell Ranch Fault trending N050, with low V_P to the southeast, where reservoir exploitation has occurred over several decades, and higher V_P to the northwest, where the reservoir is underexploited. Using coupled THM modeling, *Jeanne et al.* [2015a], interpreting tomography results from a focused seismic array around injection well Prati-32, showed that low V_P values are associated with reservoir exploitation and induced microseismicity, which is related to plastic shear failure in the numerical model. Indeed, the reactivation of preexisting fractures is expected to damage the rock mass, which then becomes progressively more fractured and deformable, facilitating reservoir

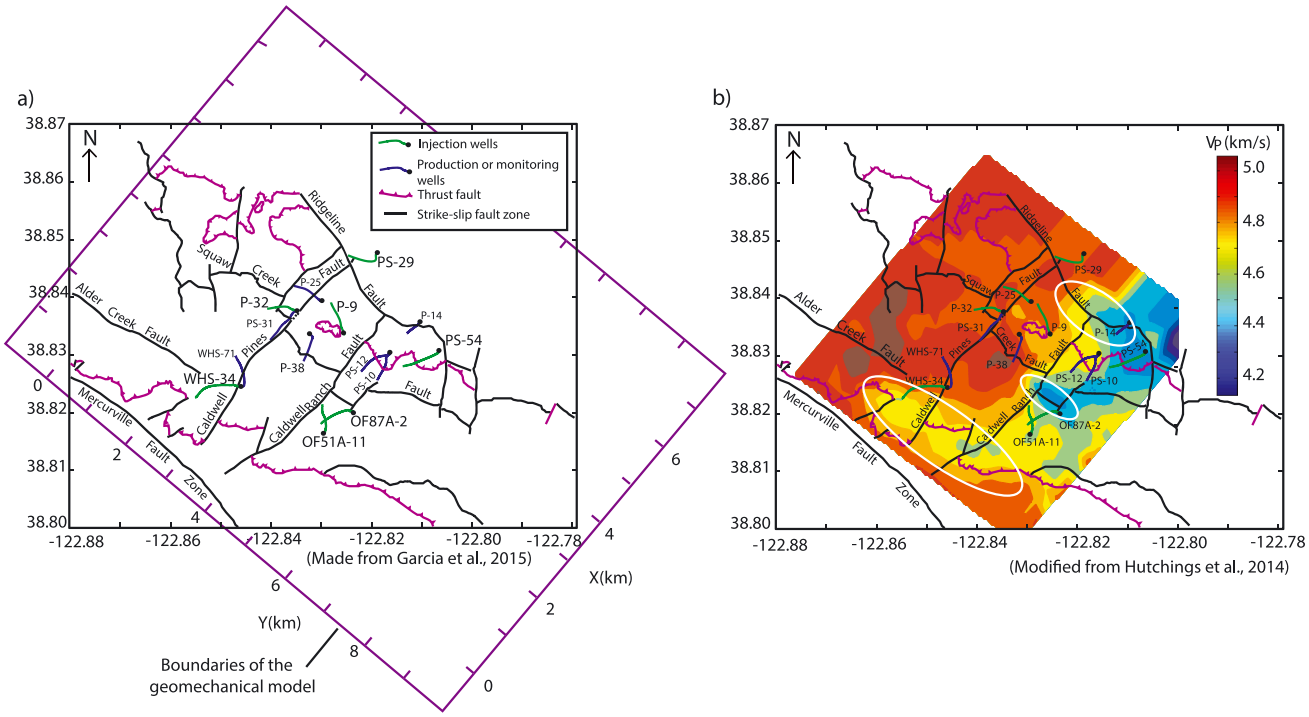

Figure 1. Comparison between (a) geological structural setting and (b) seismic tomography results in the Northwest Geysers area (made from *Garcia et al.* [2015] and *Hutchings et al.* [2014]); the white ellipses highlight low V_P anomalies extending in the N130 direction.

expansion caused by the pressure increase due to injection. The fracture shear activation, fracturing, and opening of fractures by pressure increase can cause a progressive increase in fracture porosity, which in turn could explain the observed decrease in V_P. Moreover, we observe in Figure 1b that some larger-scale low V_P anomalies appear to spread preferentially in the N130 direction (white eclipses in Figure 1b), which seems to confirm that the fault zones trending N130 favor fluid pressure diffusion through the reservoir.

In this area during the period of interest, water was injected within the normal temperature reservoir through the wells OF87A-2, OF51A-11, Prati State 54 (PS-54), and Prati State 29 (PS-29), as well as down into the high-temperature zone through the wells Prati-9 (P-9), Wildhorse State 34 (WHS-34), and Prati-32. Injection started in December 2003 in OF87A-2; in March, November, and December 2007 in OF51A-11, PS-54, and Prati-9, respectively; in April 2010 in PS-29; and in June and October 2011 in WHS-34 and P-32, respectively (Figure 2). After the beginning of 2011, four production wells were active P-14, PS-10, P-25 and PS-12 in this part of the field. Steam was produced during 12 months at P-14 at a rate around 10 kg/s, during 21 months at PS-12 at a rate around 10 kg/s, during 21 months at PS-10 at a rate around 5 kg/s, and in association with the EGS project in P-32 steam was produced during 12 months at P-25 at a rate around 8 kg/s (Figure 2). Because the production was very low compared to the injection in this area during the period of interest, steam production was removed from our modeling.

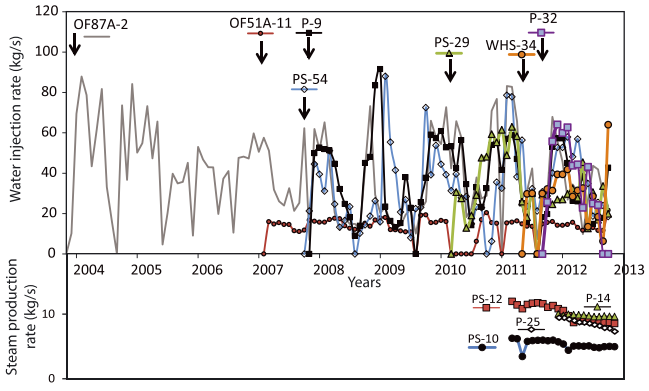

Figure 2. Injection and production history of the wells located within the Northwest Geysers area until 2013.

3. Numerical Modeling

The modeling approach used in this study leverages the knowledge and modeling related to the Northwest

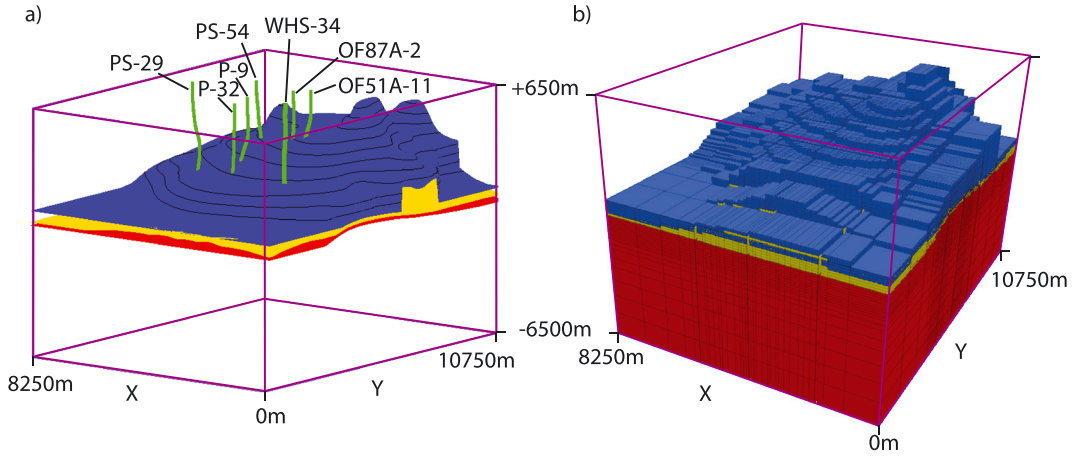

Figure 3. (a and b) Subsurface horizons of the bottom of the caprock and top of the NTR in blue, top of the HTR in yellow, and top of the felsite in red. The injection wells are green.

Geysers EGS demonstration summarized in *Garcia et al.* [2015] and *Rutqvist et al.* [2015a, 2015b]. As in the previous Geysers studies, we use the TOUGH-FLAC numerical simulator [*Rutqvist et al.*, 2002; *Rutqvist*, 2011], which has the required capabilities for modeling of nonisothermal, multiphase flow processes coupled with stress changes in a steam-dominated geothermal reservoir, such as The Geysers. In this way, the TOUGH-FLAC numerical simulator allows us to simulate the injection of cold water into a steam-saturated reservoir and to calculate changes in thermal stress caused by temperature variations and changes in effective stress caused by variations in pore pressure. In this study, we assumed that changes in stress have no impact on the reservoir porosity.

The actual 3-D model developed in this study is different from previous studies, in that it is developed to include a larger part of the Northwest Geysers and to more accurately represent the 3-D geometry of geological layers, as well as the 3-D geometry of a larger number of injection wells. The key in these simulations is to be able to investigate the stress evolution in the vicinity of injection wells at different depths and locations in the main geological units of the caprock, NTR, HTR, and felsite, with comparison to field data. This requires an accurate well geometry within the 3-D geological model. To consider the more complex 3-D geometry, we utilized the software package Groundwater Modeling System (GMS) [*Aquaveo*, 2013] to build the static geological model, which is then linked to TOUGH2 and FLAC3D for constructing consistent numerical grids. A shear zone network similar to that of *Jeanne et al.* [2014a, 2014b] is also considered in these simulations, albeit simplified to follow the grid orientations.

Calpine Corporation has developed a refined 3-D structural model in which the horizon surfaces are mapped. The subsurface horizons initially consist of a series of "markers" picked from lithology logs assigned to each well track, which are then interpolated and extrapolated to triangulated surfaces using a discrete smoothing algorithm [*Garcia et al.*, 2015]. Based on these subsurface horizons, we used GMS to construct a realistic three-dimensional geologic model of the Northwest Geysers geothermal field (Figures 3a and 3b). GMS is a graphical user environment which consists of a graphical user interface (the GMS program), providing tools for model conceptualization, mesh, and grid generation. Our model includes, from the top down, the low-permeability graywacke layer that forms the caprock for the reservoir, the isothermal steam zone (the NTR) within metagraywacke, the hornfels zone (the HTR), and the felsite that is assumed to extend downward to the magmatic heat source.

We then map this model onto a rectangular grid for use with the TOUGH-FLAC numerical simulator (Figure 3b). The numerical model extends vertically from 650 to −6500 m (elevation relative to sea level) and 8250×10750 m horizontally. At the bottom of the domain in the felsite, we impose a constant temperature, constant saturation, and low-permeability boundary. Laterally, we set no-flow boundaries (no mass or heat flow), while at the top we use a fully aqueous-phase-saturated constant atmospheric pressure boundary condition. The initial thermal and hydrological conditions (vertical distributions of temperature, pressure, and liquid saturation) are established through steady state, multiphase flow simulations. The initial steam

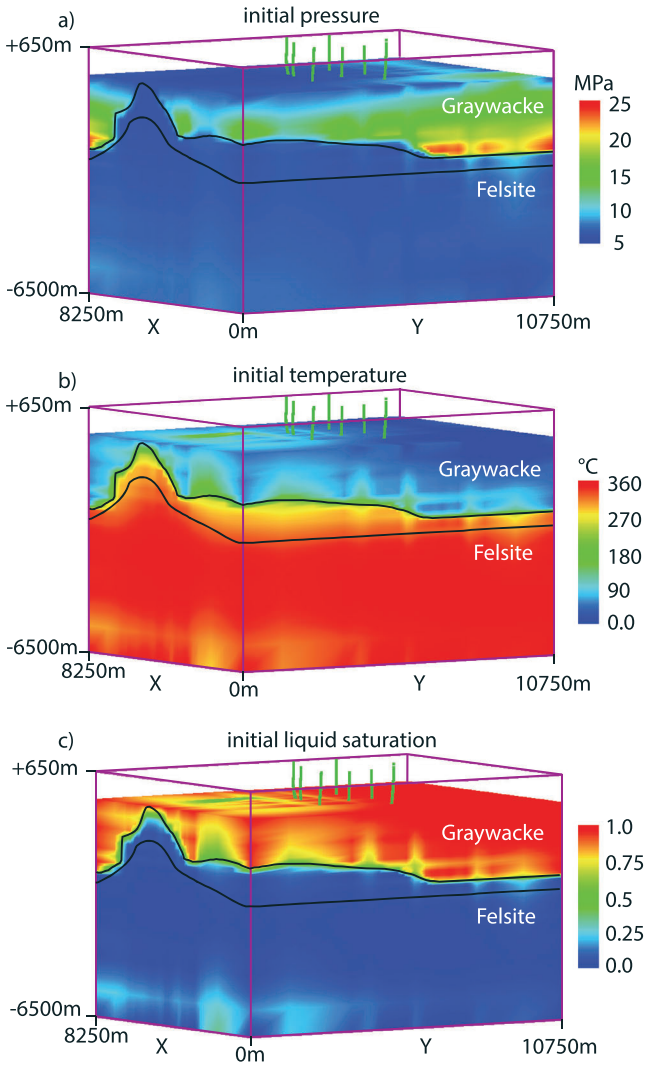

Figure 4. Initial distributions of (a) pressure, (b) temperature, and (c) liquid saturation. The black lines represent the top of the steam zone and the top of the felsite.

pressure within the reservoir is about 6 MPa, whereas the pressure outside the sealed reservoir is hydrostatic (up to 25 MPa at the base of the caprock) (Figure 4). The initial reservoir temperature in the NTR is approximately 240°C down to the HTR and then gradually increases up to 370°C toward the bottom boundary at a depth of −6.5 km (the 370°C is the upper temperature limit of the TOUGH module used). On the top boundary, the ground surface is free to move, whereas stress at the other boundaries follows the lithostatic gradient.

We simulate the rock mass as an equivalent continuum with implicit representation of fractures, whereas the fault zones are explicitly represented with different hydraulic properties. In such an approach, the input hydraulic properties represent fracture permeability and porosity. The fault zones trending N130 are assumed to have a higher permeability and a higher porosity than the host rock, and inversely, the fault zones trending N050 are assumed to have a lower permeability and a lower porosity than the host rock. The hydraulic, mechanical, and thermal properties used in our model are summarized in Table 1.

The simulated wells consist of a vertical, 500 m long open hole section, where fluid flow and heat exchange are allowed with the surrounding rock. Water is injected at 90°C at the top of the 500 m section. As observed on the field, the simulated wells inject water at different depths. For example, the bottom of the injection wells OF87A-2, Prati-9, and Prati-32 are respectively located at about −1900 m, −2050 m, and −2500 m (below sea level) in the field and in our model.

Common to all the simulations carried out during this study, an initial normal stress regime ($S_V \geq S_{Hmax} > S_{hmin}$) is imposed throughout the models at the beginning of the simulations. S_V is equal to the lithostatic stress.

Table 1. Properties Used in the 3-D Model

	Caprock	NTR	HTR	Felsite	Fault N130	Fault N050
Young's modulus (GPa)	28	28	28	28	28	28
Poison's coefficient (−)	0.25	0.25	0.25	0.25	0.25	0.25
Thermal conductivity (W/m°C)	3.2	3.2	3.2	3.2	3.2	3.2
Thermal expansion ($°C^{-1}$)	1.E−05	1.E−05	1.E−05	1.E−05	1.E−05	1.E−05
Specific heat (J/kg/°C)	880	880	880	880	880	880
Permeability (m^2)	1.0E−25	1.0E−14	5.0E−15	5.0E−16	1.0E−14	1.0E−20
Porosity (%)	5.0	5.0	2.0	1.0	3.0	3.0

S_{Hmax} is oriented N020E [*Boyle and Zoback*, 2014] and $S_{hmin} = 0.34 \times S_V$ [*Jeanne et al.*, 2014c]. Because the temperature is too high (up to 400°C) for the packers, no mini-frac test have never been done in the HTR at The Geysers to the best of our knowledge. This value of 0.34 was estimated through a series of 3-D THM simulations focused on the injection well P-32 [*Jeanne et al.*, 2014c] by comparing the observed temporal and spatial distribution of microseismic activity during reservoir stimulation and the calculated shear reactivation of preexisting fractures inferred from simulated elastoplastic mechanical responses in a short fault zone network. This low value of S_{hmin} means that the rock mass is initially in a stress state close to shear failure, and small perturbations of the stress field can cause a fracture to move. This initial stress condition is consistent with previous studies, where the concept of a critically stressed rock mass at The Geysers has been successfully applied [*Rutqvist et al.*, 2015b; *Jeanne et al.*, 2015b; *Rutqvist and Oldenburg*, 2008] and dates back to rock mechanics studies conducted in the early 1980s [*Lockner et al.*, 1982]. In the "reference simulation," $S_{Hmax} = 0.99 \times S_V$, and in two other simulations performed during a sensitivity analysis $S_{Hmax} = 0.90 \times S_V$ and $S_{Hmax} = 0.95 \times S_V$. The orientation of the stress tensor is extracted from the simulation results once every month. We extract the nine components that completely define the 3-D state of stress given by matrix A (equation (1)), and we calculate its eigenvectors to find the vector coordinates of σ_1, σ_2, and σ_3. S_{Hmax} magnitude is calculated using equation (2) [*Jaeger et al.*, 2012], where θ is S_{Hmax} orientation relative to north. In our model, z is vertical, and the x and y axes are oriented N050 and N130, respectively.

$$\sigma = \begin{pmatrix} \sigma xx & \sigma xy & \sigma xz \\ \sigma yx & \sigma yy & \sigma yz \\ \sigma zx & \sigma zy & \sigma zz \end{pmatrix}, \tag{1}$$

with $S_V = \sigma_{zz}$.

$$S_{Hmax} = \sigma_{xx} \cos^2 \theta + 2\ \sigma_{xy} \sin\theta \cos\theta + \sigma_{yy} \sin^2 \theta \tag{2}$$

4. Modeling Results

4.1. Evolution of the Stress Tensor Over the Northwest Geysers Area From 2003 to 2012

Figure 5 presents pressure and temperature distribution, and the stress tensor distribution at the end of 2012, after 9 years of injection. The stress tensor is described by three angles: β, α, and θ. β is the angle between the vertical stress and σ_1, α is the angle between the vertical stress and σ_2, and θ represents the horizontal rotation of S_{Hmax} (θ). The results in Figure 5 are presented for map views at three different depths, inside the NTR ($z = -1900$ m), the HTR ($z = -2316$ m), and the felsite ($z = -3031$ m). PS-29 is the only injection well which is not intersected by these map views (the bottom of PS-29 is located at $z \approx -1700$ m). However, because injection in PS-29 has an impact on the stress state, its location is given on Figure 5d. In the simulation, calculated changes in pore pressure occur at a large scale (several kilometers) and deep inside the felsite (Figures 5a–5c). Because at most of the wells, water is injected within the NTR, it is where most of the changes in temperature occur, though limited to just a few hundred meters around the injection wells (Figures 5d–5f). The areas where the temperature decreases are those which are liquid saturated by the injected water.

Only changes in temperature (and not changes in pressure) seem to affect the orientation of S_{Hmax}, which slightly rotates in the vicinity of the injection wells, where the temperature drops (Figures 5g and 5h). S_{Hmax} rotates up to ≈13° close to the wells, but the rotation quickly decreases below 10° at some distance from the wells. No change in S_{Hmax} orientation is observed inside the felsite, where no significant change in temperature is calculated.

σ_1, which is initially vertical ($= S_V$), is much more influenced by the injection. Figures 5j–5o show the rotation angles of σ_1 (β) and σ_2 (α) relative to the vertical plane inside the NTR, the HTR, and the felsite. The calculated rotations in Figures 5j–5l are the exact opposite of the rotations in Figures 5m–5o. This means that σ_1 rotates from vertical toward the σ_2 (S_{Hmax}) direction, whereas no rotation of σ_3 (S_{hmin}) is calculated. We also observe that the rotation of σ_1 occurs at a larger scale below the injection zones, even if no change in temperature is calculated at such a depth (as for the wells OF87A-2, OF51A-11, and PS-29 (Figures 5d, 5e, 5j, and 5k)). The perturbations in stress tensor orientations propagate several kilometers in the σ_2 direction, but only 1 km in the σ_3 direction (Figures 5j and 5k).

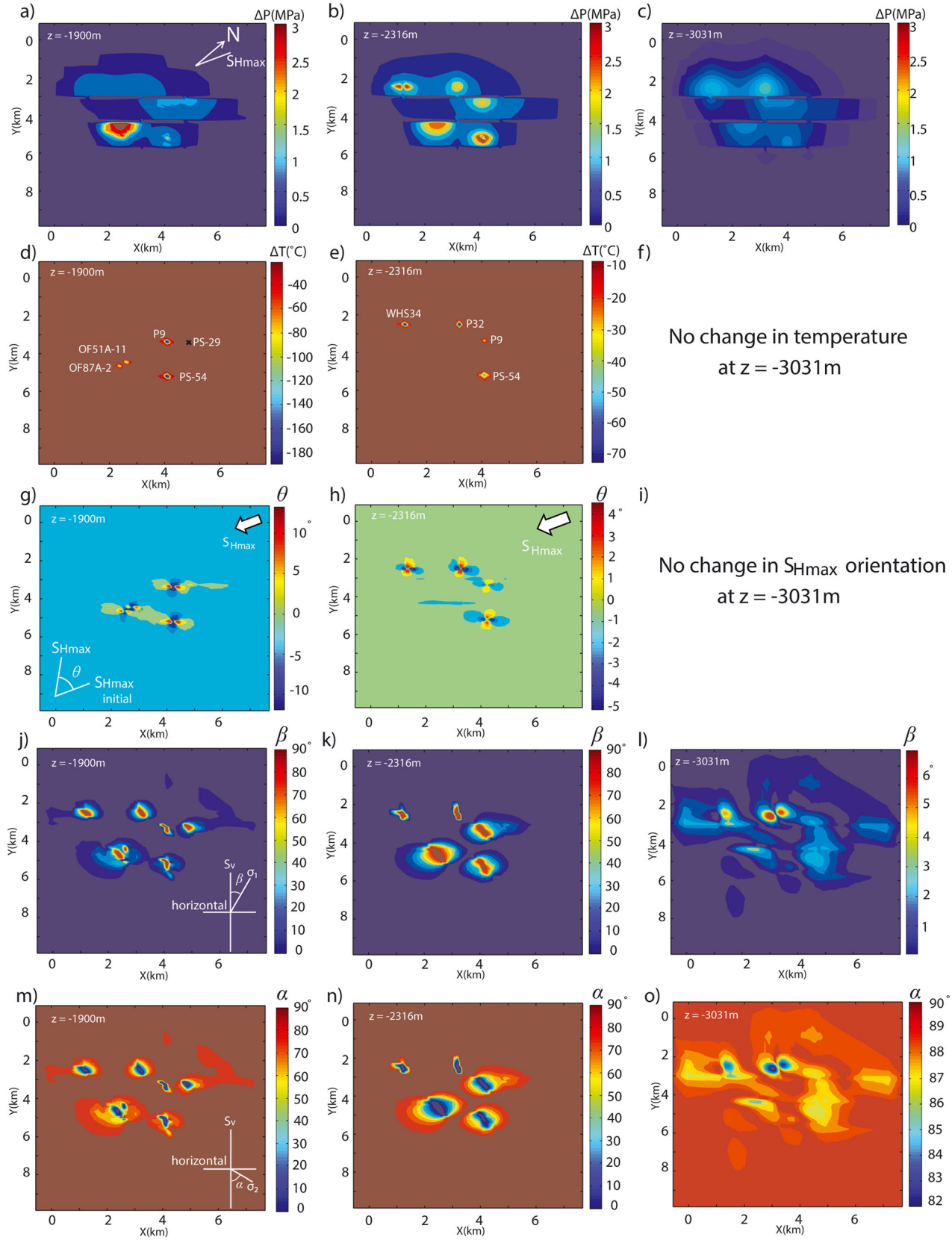

Figure 5. Calculated (a–c) pressure and (d–f) temperature change distribution, (g–i) orientation of S_{Hmax}, and vertical rotation of (j–l) σ_1 and (m–o) σ_2 inside the NTR, the HTR, and the felsite at the end of 2012.

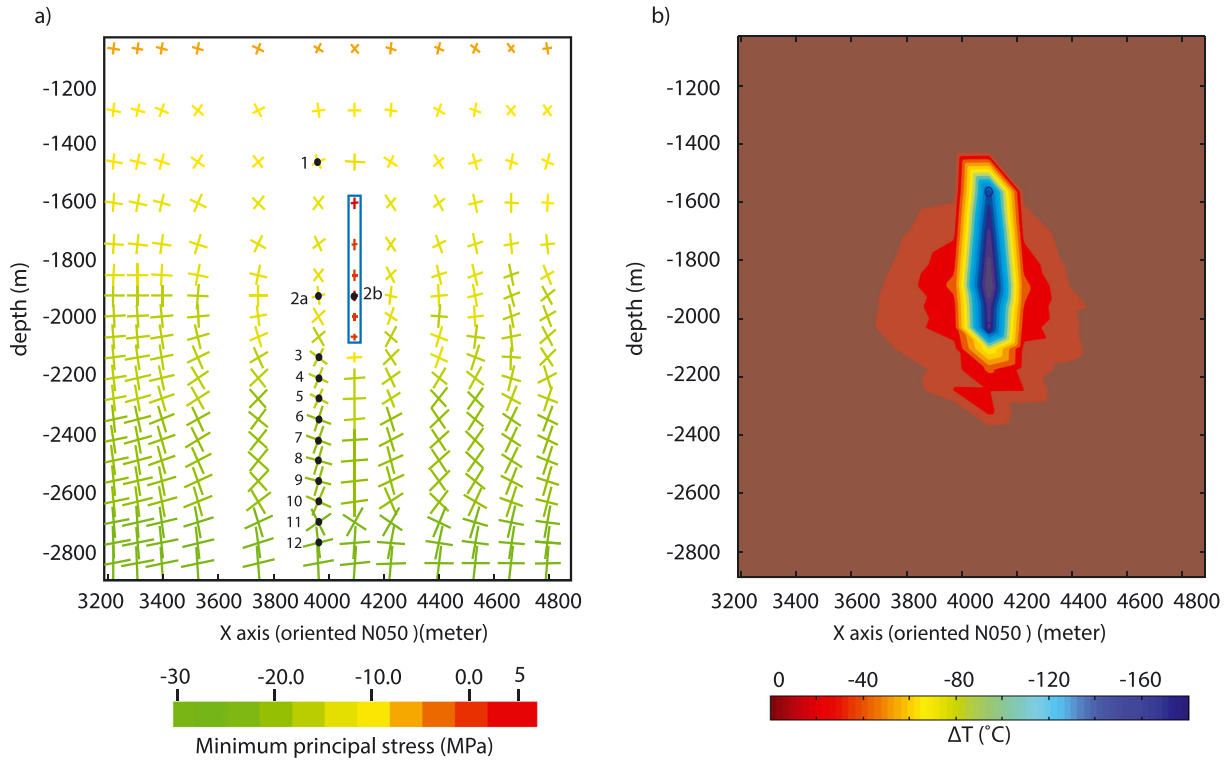

Figure 6. (a) Stress tensor and (b) temperature distribution around Prati-9 after 5 years of injection (end 2012) with the location on the different control points used during this study (From CP1 to CP12) (Figure 6a). The rectangle in Figure 6a corresponds to the open hole.

4.2. Evolutions of S_{Hmax} and S_V Around Prati-9 From 2007 to 2012

To better understand the distribution and the temporal evolution of the stress tensor around an injection well, we focus our study on the injection well Prati-9, where injection started in December 2007. In this case, we investigated the local stress response to fluid injection over a 5 year period. Figures 6a and 6b present the stress tensor and temperature distribution around Prati-9 at the end of 2012 along a cross section oriented N050. As mentioned, the area where temperature drops corresponds to the liquid-saturated zone formed after 5 years of injection. We selected several control points where the 3-D rotation of the stress tensor was calculated. Relative to the injection zone, these control points were located as follows: above (CP1), around (CP2a), inside (CP2b), and below (CP3 to CP12) (Figure 6a).

4.2.1. Evolution of the Stress Tensor Over Time

Figure 7 presents changes in pressure, temperature, and state of stress, from the end of 2003 to the end of 2012, at point CP2b near Prati-9 (Figure 6a), where the highest changes in temperature were calculated. In this case, for the sake of clarity, we present results obtained during a simulation in which the initial stress state is $S_{Hmax} = S_V \times 0.95$ instead of $S_{Hmax} = S_V \times 0.99$. The general behavior is exactly the same, but changes in the stress tensor at CP2b are more visible. It clearly appears that injections in OF87A-2, OF51A-11, and PS-54 from 2003 to December 2007 have no impact on the pressure, temperature, and state of stress around Prati-9. Then, following the beginning of injection in Prati-9, changes in steam pressure occur quickly and are strongly affected by the seasonal variations in the injection rate. The pressure decreases during summer when the injection rate decreases and peaks during winter when the injection rate is at its peak level (Figure 7a). Inversely, the injection-induced cooling is a much slower process unaffected by the seasonal variations in the injection rate. Changes in temperature are more persistent, which result in a progressive decrease in temperature over the years (Figure 7b). The thermal processes associated with this temperature drop cause a progressive cooling-stress reduction (Figure 7c), which is higher in the direction of the water flow. The gravity flow causes a higher decrease in the S_V (equal to σ_1 at t_0) than in the S_{Hmax} (equal to σ_2 at t_0). The consequence is that after 7–8 months of injection, the S_V becomes equal to S_{Hmax} (t_1 in Figure 7c; at that moment, $\sigma_1 = \sigma_2$). After t_1, because S_V keeps decreasing more than S_{Hmax}, S_V becomes lower than S_{Hmax}.

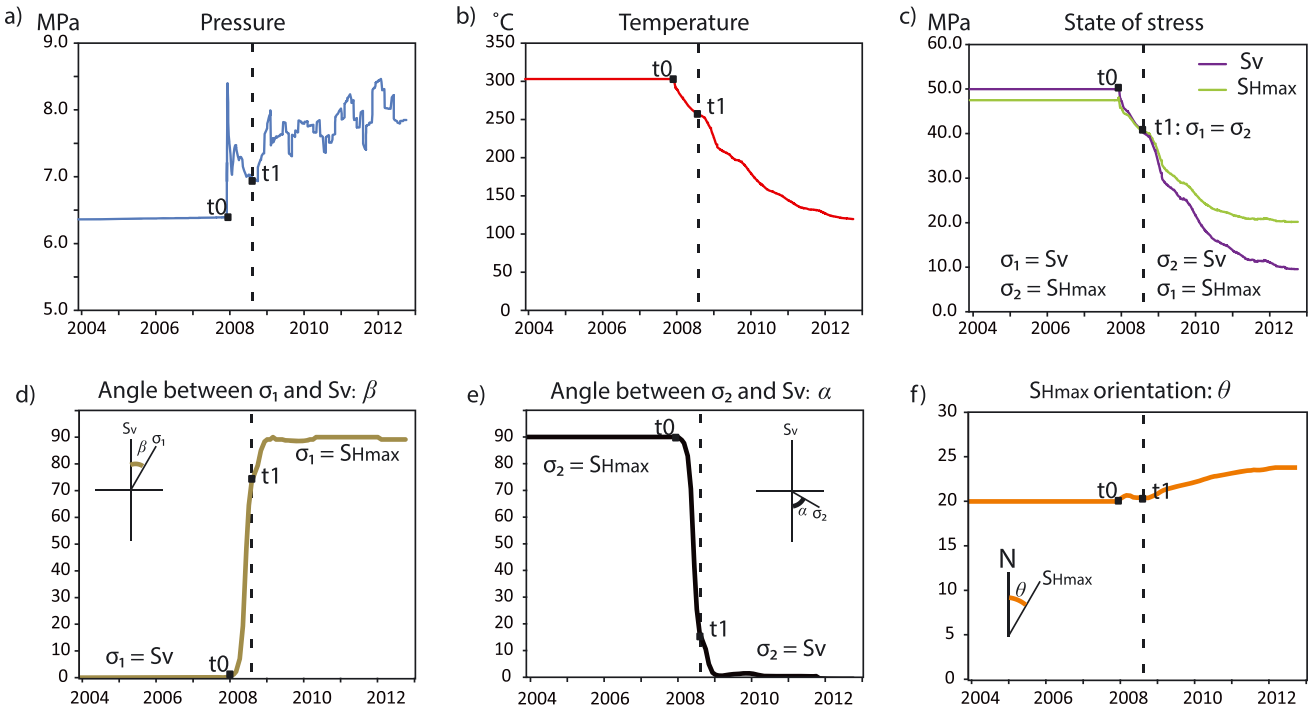

Figure 7. Calculated evolution of (a) fluid pressure, (b) temperature, (c) σ_1 and σ_2, (d and e) the angle between σ_1 and σ_2 with the vertical, and (f) the orientation of S_{Hmax} in the area where the highest changes in temperature occur (Control Point CP2b in Figure 6a).

This results in an inversion of the local stress state (Figures 7d and 7e), from a normal stress regime ($S_V \geq S_{Hmax} > S_{hmin}$) to a strike-slip regime ($S_{Hmax} \geq S_V > S_{hmin}$). At the same time, the rotation of S_{Hmax} (σ_2 until t_1 and σ_1 after t_1) is very small (as shown in Figure 7f, only up to 4° after 5 years of injection).

Figure 8 presents changes in pressure, temperature, and state of stress at three control points located above, beside, and below Prati-9 (CP1, CP2a, and CP3, respectively, in Figure 6a). Because injections in the surrounding wells before 2008 have a very slight effect on the state of stress around Prati-9, we focus on the results calculated after the beginning of the injection in Prati-9. In this simulation, we assign initial stress conditions of $S_{Hmax} = S_V \times 0.99$.

4.2.1.1. Above the Injection Well (CP1, $z = -1420$ m)

This is where the smallest changes in pressure and temperature are calculated, with $\Delta P \approx 0.6$ MPa and $\Delta T \approx 0$°C (Figure 8a). However, it is also where the largest rotation of σ_1 is calculated, with a rotation up to ~70° after 5 years of injection (Figure 8b). This phenomenon occurs quickly, with a rotation of 60° after only 260 days of injection, and then slowly evolves over the next 4 years. As noted previously, σ_1 rotates toward the σ_2 direction, which in turn rotates by the same angle relative to the horizontal plan (Figure 8b). Finally, above the injection well, the horizontal rotation of S_{Hmax} is very small (only a few degrees) (Figure 8c). Figure 6a shows that these changes in the stress tensor above the injection well are localized and do not extend far away from the well. These rotations result from (i) a reduction in vertical stress caused by the stress reduction within the cooling area and (ii) the associated stress redistribution above the cooling area (Figure 8d) as shown in *Rutqvist and Oldenburg* [2007]. This last point is discussed in the sensitivity analysis.

4.2.1.2. Beside the Injection Well (CP2a, $z = -1886$ m)

Note that compared to CP1 and CP3, this is the location where the largest changes in temperature are calculated ($\Delta T \sim -50$°C) (Figure 8e) and also where the calculated rotation of σ_1 is the smallest (up to 14°) and follows the seasonal variations in the injection rate (Figure 8f). Every year, the largest rotation of σ_1 occurs during winter, when the injection rate is at its peak level. On the other hand, this location is where the largest changes in S_{Hmax} direction occur, with a horizontal rotation up to 16° (Figure 8g). These changes in stress tensor direction are mostly caused by stress reduction. Beside the injection well, the liquid zone and (thus) the cooling area tend to expand laterally, which results in a vertical stress reduction almost equal to the horizontal stress reduction (Figure 8h). Over the years, these small differences between S_V and S_{Hmax} result

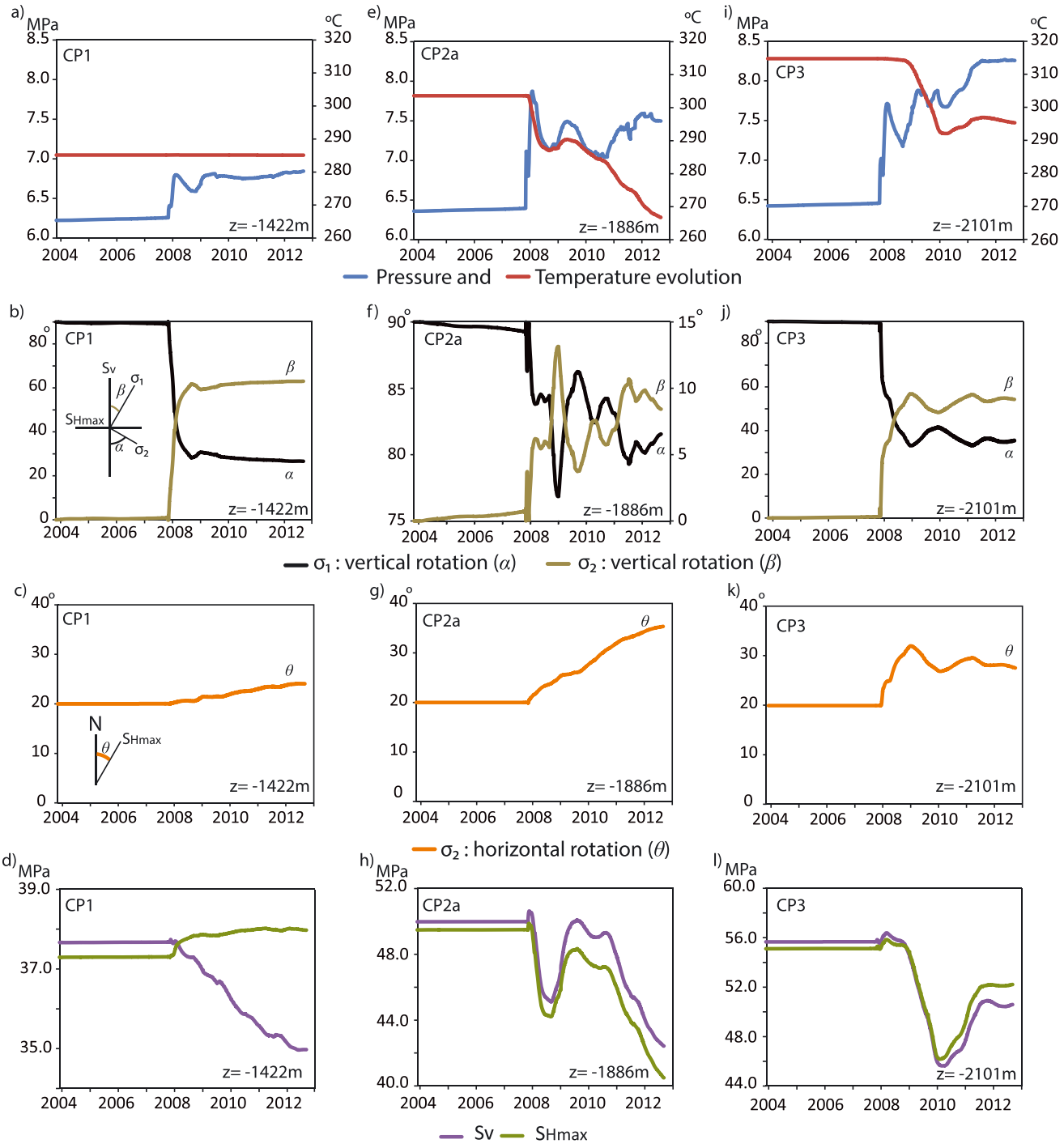

Figure 8. Calculated evolution changes in fluid pressure, temperature, rotation angles of σ_1 and σ_2 relative to the horizontal plane, and rotation of S_{Hmax} at monitoring points (a–d) above, (e–h) beside, and (i–l) below the injection zone.

in small and progressive variations in the σ_1 direction. Moreover, the seasonal variations of the injection rate produce higher cooling during winter (at high injection rate) than during summer (at low or null injection rate). Indeed, when the injection rate decreases or stops during the summer, the temperature stops dropping and increases slightly (Figure 8e). The consequence is that during winter (at injection peak), S_V decreases slightly more than S_{Hmax} (Figure 8h), leading to the rotation of σ_1; during summer, S_V increases slightly more than S_{Hmax}, and the stress tensor rotates back toward its initial value (Figure 8f).

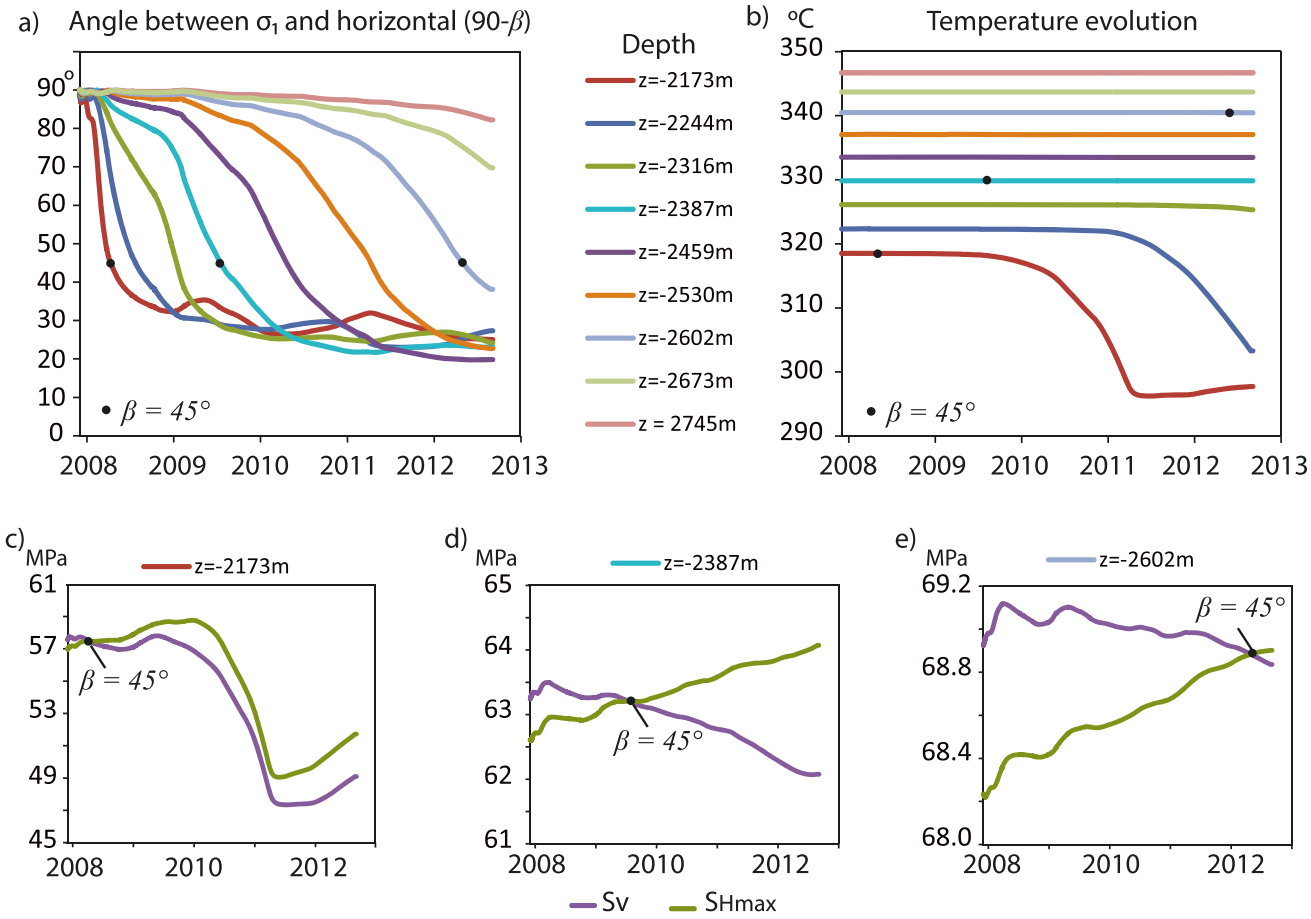

Figure 9. Calculated evolution of (a) σ_1 orientation and (b) temperature at nine control points located between 173 m and 745 m below the injection well. Calculated evolution of S_{Hmax} and S_V at (c) $z = -2173$ m, (d) $z = -2387$ m, and (e) $z = -2602$ m.

4.2.1.3. Below the Injection Well (CP3, $z = -2101$ m)

At CP3, the temperature decreases slightly ($\Delta T \approx -20$°C), and changes in pressure are higher than those calculated at CP1 (up to ΔP of ~1.8 MPa) (Figure 8k). However, the rotations of the stress tensor are very similar. In less than 1 year, σ_1 rotates as much as 60° toward the σ_2 direction and reaches a quasi-equilibrium state, which is slightly influenced by changes in temperature. At the same time, changes in the S_{Hmax} direction are less than 10°.

Figure 9a shows, at nine control points located below the injection well Prati-9 (CP4 to CP12 in Figure 6a), how far and how quickly changes in σ_1 orientation propagate below the injection zone, which is located between −1550 and −2050 m below sea level in our simulation. We observe that (i) the perturbations of the stress tensor propagate much farther than the temperature variations and (ii) from the bottom of the injection well to 800 m deeper, the orientation of σ_1 changes from vertical (90°) to almost horizontal (20°), creating a strike-slip stress regime just below the well and a normal stress regime 800 m deeper. We also notice that the part of the reservoir subject to a strike-slip stress regime (σ_1 oriented 20°) deepens at a rate of approximately 100 m/yr. Figures 9c–9e present the evolution of S_V and S_{Hmax} at three control points below the injection well: CP4 ($z = -2173$ m), CP7 ($z = -2387$ m), and CP10 ($z = -2602$ m). It appears that the stress rotation is caused by a decrease in S_V (due to the vertical stress drop in the upper part, inside the cooling area) and an increase in S_{Hmax} caused by stress redistribution around the cooled area.

4.2.2. Sensitivity Analysis

4.2.2.1. Sensitivity to Stress State

We perform two other simulations to investigate sensitivities to initial stress conditions (S_V/S_{Hmax} ratio). Figure 10 shows the rotations of σ_1 calculated and the evolution of S_V and S_{Hmax} at the control points

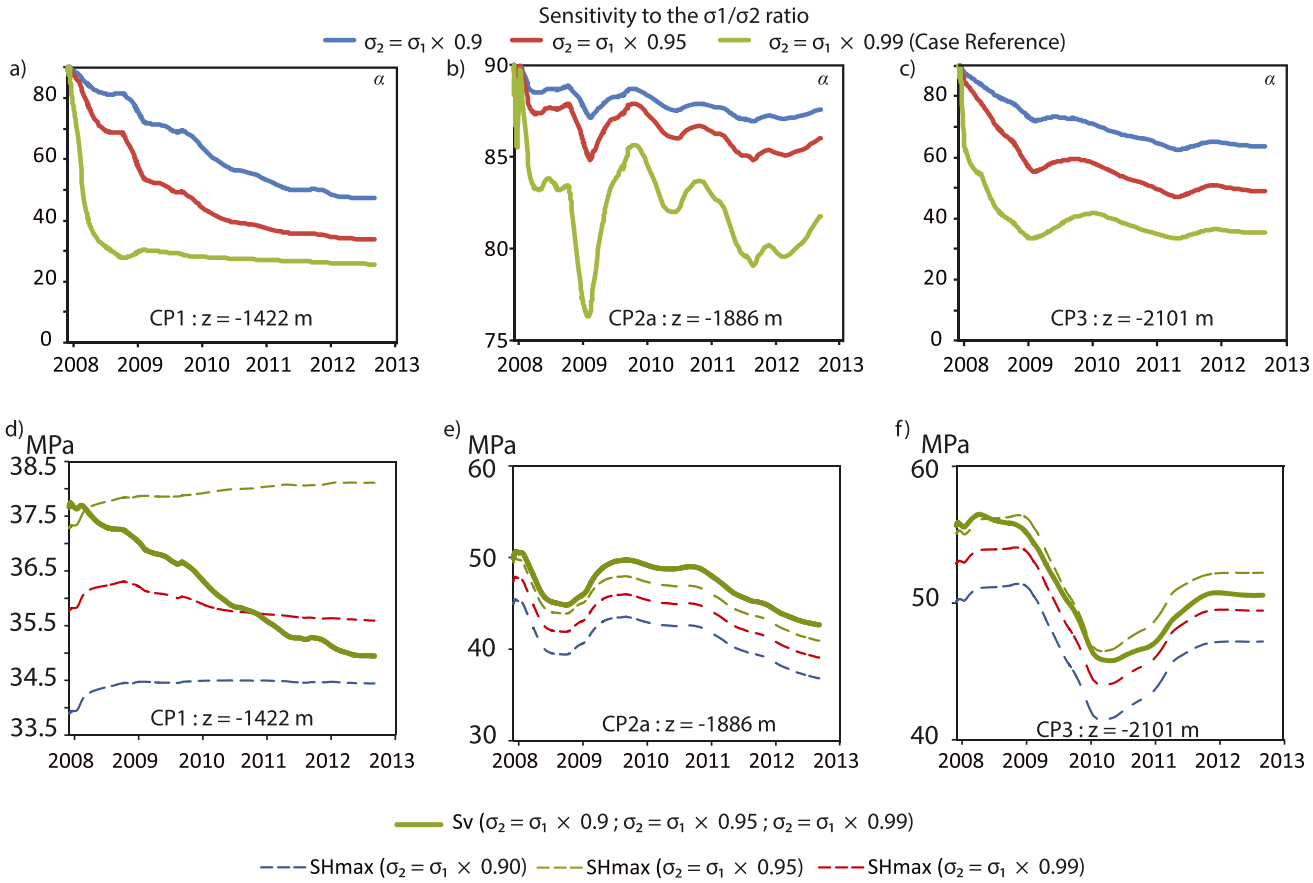

Figure 10. Sensitivity to state of stress on σ_1 orientation and evolution of S_V and S_{Hmax} (a and d) above ($z = -1422$ m), (b and e) beside ($z = -1886$ m), and (c and f) below ($z = -2101$ m) the injection zone.

located above (CP1, $z = -1420$ m), beside (CP2a, $z = -1886$ m), and below (CP3, $z = -2101$ m) the injection zone. In these tests, we assign the same initial S_V, so only S_{Hmax} is varied in the three different simulations. We observe that the closer to 1 the S_V/S_{Hmax} ratio is, the larger the injection-induced rotation of σ_1 (Figures 10a–10c). For a S_V/S_{Hmax} ratio close to 1, only small variations in S_{Hmax} are needed for S_{Hmax} to become equal to or higher than S_V, and therefore, small variations in S_{Hmax} result in a significant rotation of σ_1. From these observations, we can state that if S_{Hmax} is much higher than S_{hmin}, even if horizontal stresses increase uniformly as a result of pressure effects, σ_1 will always rotate toward the σ_2 orientation.

4.2.2.2. Sensitivity to Thermal Processes

The HM simulation does not show any rotation in σ_1 above or below the injection zone (lower than 3° after 5 years, Figures 11a and 11c). This confirms that thermal processes, and thus the shrinkage of the reservoir within the cooling area, lead to stress tensor rotation above and below the cooling area. Also in the HM simulation, at the injection depth (Figure 11b), there is a progressive rotation of σ_1 up to 5° (from 90° to 85°) after 5 years of injection. Such behavior is caused by reservoir expansion and the confining stress acting inside the reservoir. During injection, the pressure increases, leading to reservoir expansion, which is resisted, to some extent, by the adjacent rock. As the rock expands, the vertical and horizontal compressive stresses imposed by the surrounding rock would increase. However, because the topographic surface is free to move, the vertical confinement is less important than the horizontal confinement; consequently, S_V increases less than S_{Hmax}.

In the THM simulation, the rotation of the stress tensor is much larger than in the HM simulation. As explained above, this behavior is caused by development of the cooling area and its associated stress reduction. We also observe that above the cooling area, S_{Hmax} is higher in the THM simulation than in

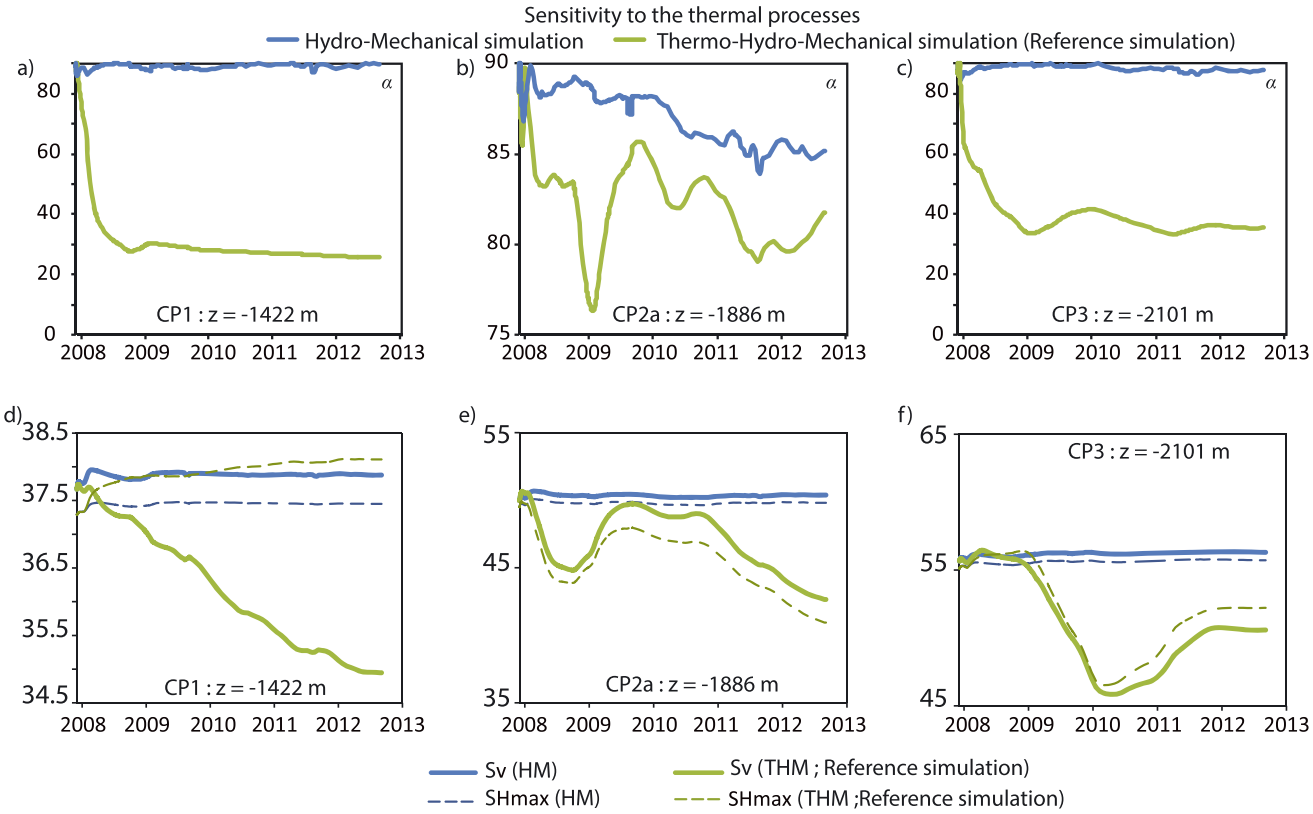

Figure 11. Sensitivity to thermal processes on σ_1 orientation and evolution of S_V and S_{Hmax} (a and d) above ($z = -1422$ m), (b and e) beside ($z = -1886$ m), and (c and f) below ($z = -2101$ m) the injection zone.

the HM simulation (Figure 11d). This means that the increase in S_{Hmax} in the THM simulation is largely controlled by stress redistribution above and below the cooling area, as shown in *Rutqvist et al*. [2007].

5. Discussion

5.1. Comparison With the Theory of Thermoelasticity

The theory of thermoelasticity accounts for the effect of changes in temperature on the stresses and displacements in a body. The basic assumption of linear thermoelasticity is that if the rock is subjected to both a temperature change and an applied stress state, then the resulting strain is the sum of the thermal strain and the stress-induced strain [*Jaeger et al*., 2012]. These stress-strain relations can be expressed in terms of the shear modulus (G) and Poisson's ratio (υ) and written in a matrix form as

$$\varepsilon = \frac{1}{2G}\sigma - \frac{\upsilon}{2G(1+\upsilon)} tr(\varepsilon) I - (\alpha \Delta T) I \tag{3}$$

with $tr\,(\varepsilon) = \varepsilon_{xx} + \varepsilon_{yy} + \varepsilon_{zz}$.

ε is the strain, σ the stress tensor, I the 3×3 identity tensor, α the linear coefficient of thermal expansion, and ΔT the temperature variations. Taking the trace of both sides of equation (3) yields

$$tr(\varepsilon) = \frac{\Delta \sigma_n}{K} - 3\alpha \Delta T \tag{4}$$

with $\Delta \sigma_n$ the mean normal stress variations and K the bulk modulus. This indicates that 3α is the volumetric thermal expansion coefficient. An increase in temperature will cause a negative bulk strain, which means that the bulk volume will increase, whereas a decrease in temperature will cause the bulk volume to decrease. It is why in our simulation, the injection of cool water inside a hot reservoir causes shrinkage of the rock inside the cooling area.

The equations for the stresses in terms of the strains are found by inverting equations (3) and (4) and can be written as

$$\begin{aligned}\sigma_{xx} &= 2G\varepsilon_{xx} + \lambda\left(\varepsilon_{xx} + \varepsilon_{yy} + \varepsilon_{zz}\right) + 3\ \alpha K\Delta T\\ \sigma_{yy} &= 2G\varepsilon_{yy} + \lambda\left(\varepsilon_{xx} + \varepsilon_{yy} + \varepsilon_{zz}\right) + 3\ \alpha K\Delta T\\ \sigma_{zz} &= 2G\varepsilon_{zz} + \lambda\left(\varepsilon_{xx} + \varepsilon_{yy} + \varepsilon_{zz}\right) + 3\ \alpha K\Delta T\\ \sigma_{xy} &= 2G\varepsilon_{xy}, \tau_{xz} = 2G\varepsilon_{xz}, \tau_{xz} = 2G\varepsilon_{yz}\end{aligned} \tag{5}$$

with λ the Lame parameter. Equation (5) shows that thermally induced stresses are not caused by temperature changes per se but rather by the combination of a change in temperature and a mechanical restraint that inhibits free expansion or contraction of the rock [*Jaeger et al.*, 2012].

In our simulation, both the vertical trajectory of the injection zone and the gravity flow result in the appearance of a cooling area with an elongated shape in the vertical direction where the stresses decrease. Because of this elongated shape in the vertical direction, the vertical confining stress inside the cooling area decreases significantly, and so the contraction of the rock is less restricted in the vertical direction than in the horizontal direction (equation (5)). It is why we observe a stress reduction more important in the direction of the gravity flow which causes the rotation of the stress tensor. In the same way, the horizontal confining stress is less important in S_{hmin} direction than in S_{Hmax} direction. Therefore, changes in stress in S_{hmin} direction have higher amplitude than those in S_{Hmax} direction (Figure 5k). However, because $S_V \approx S_{\text{Hmax}}$, small variations in S_{Hmax} are needed for S_{Hmax} to become equal to or higher than S_V; the rotation of σ_1 toward S_{Hmax} occurs over a large distance (Figure 5k).

5.2. Comparison With Studies Based On the Inversion of Focal Plane Mechanism

During this study, we analyzed the effect of injection on the stress tensor orientation in part of the Northwest Geysers over almost a decade. As observed by *Oppenheimer* [1986] and *Boyle and Zoback* [2014], we find that the direction of S_{Hmax} around the injection wells stays very similar to the regional orientation of S_{Hmax}. Indeed, except for a rotation in S_{Hmax} of 16° very close the injection well, we observe only a slight rotation in S_{Hmax} of less than 10° (Figure 5). Such a small angle falls within the nodal plane uncertainty of the focal mechanisms and therefore may be not detected by the analyses of focal plane mechanisms.

We also studied in detail the evolution of the stress tensor around injection well Prati-9 during 5 years of injection. Consistent with observations from focal plane mechanisms by *Martínez-Garzón et al.* [2013], we calculated significant rotations in the orientation of the main principal stress (σ_1) in response to the seasonal changes in the fluid injection rates, with σ_1 rotating from vertical toward the σ_2 direction. *Martínez-Garzón et al.* [2013] highlighted that σ_1 tilted by approximately 20°, and this value is similar to our results, where σ_1 tilted by up to 14° at the injection depth. However, *Martínez-Garzón et al.* [2013] showed that after peak injection and when the injection rate is at its lowest level, the σ_1 axis rotates back toward close to its initial vertical position. Although our simulation showed seasonal variations in σ_1 rotation, the σ_1 axis did not rotate back as close to the initial vertical position. This difference can be explain as follows: as shown in Figure 8, σ_1 axis rotates back because the temperature stops dropping and increases slightly when the injection rate is at its lowest level. In our model, the initial temperature in the HTR is 370°C (which corresponds to the upper temperature limit of the TOUGH module used), but temperatures up to 400°C have been identified in P-32 [*Garcia et al.*, 2015]. Therefore, when the injection rate is at its lowest level, temperature can increase a little bit more than in our simulation and σ_1 rotates back up to its initial vertical position.

5.3. Impact on the Longer-Term Microseismic Evolution Around Active Injection Wells

At The Geysers, *Lipman et al.* [1978] and *Hulen et al.* [1995] noted that fractures observed in core samples are typically high angle to near vertical, and *Boyle and Zoback* [2014] showed that most of the induced seismic events occur along one set of fractures near vertical and trending ±30° to S_{Hmax}. The rock formations are critically stressed [*Lockner et al.*, 1982; *Rutqvist et al.*, 2015a], and small perturbations in steam pressure caused by injection are the main mechanism of induced microseismicity [*Jeanne et al.*, 2014c]. The induced seismic clouds are mostly located below the injection wells, whereas the pressure diffusion within the reservoir occurs in every direction. For example, Figure 12 presents the microseismic activity evolution induced by the injection of cold water in OF87A-2 and OF51A-11 (Figure 12a), in Prati-9 and Prati State 29 (Figure 12b), and in Prati-32 (Figure 12c). The bottom of these injection wells is located at −1900 m, −2000 m, −2050 m, −1700 m, and −2600 m below sea level, respectively (represented by the orange stars

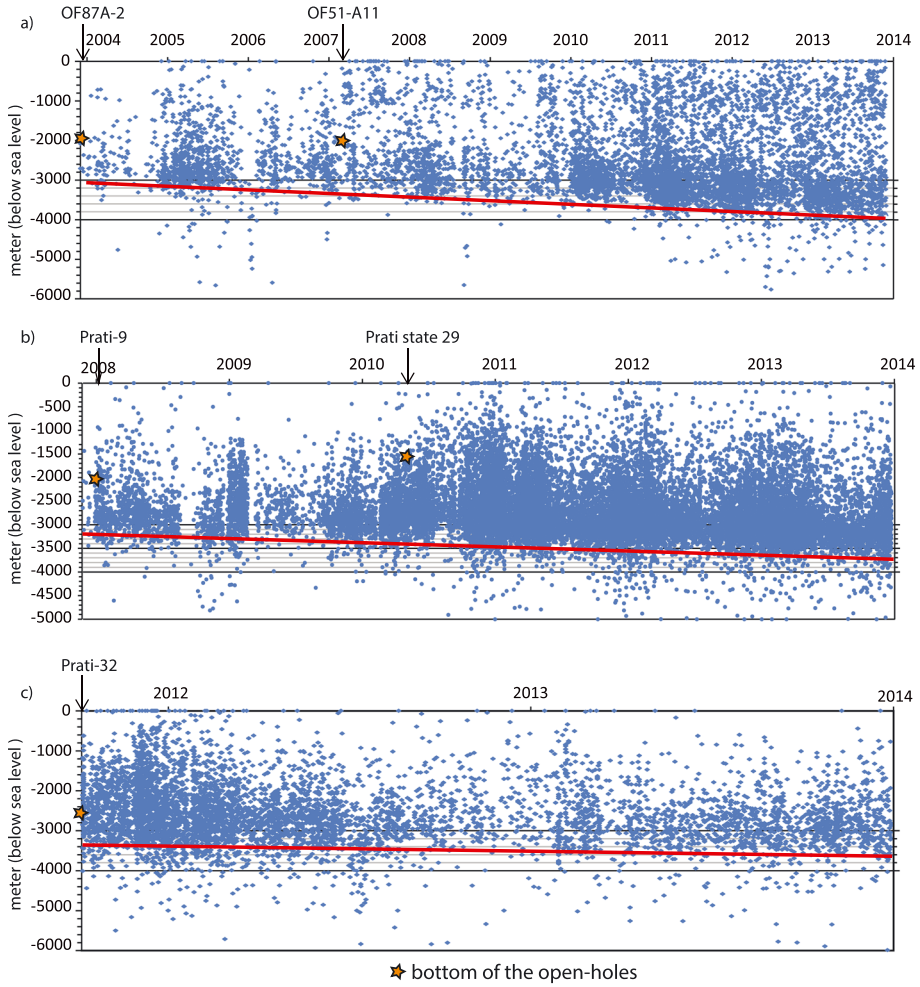

Figure 12. Microseismicity evolution around the injection wells: (a) OF87A-2 and OF51A-11, (b) Prati-9 and Prati State 29, and (c) Prati-32: depth versus time. The orange stars represent the bottom of the open hole.

in Figure 12), and most of the seismic activity is located at −2000 m to −4000 m below sea level. Also, Figure 12 shows a progressive and slow deepening of the induced seismic events below these injection wells (red lines in Figure 12). Below OF87A-2/OF51A-11, the bottom of the induced seismic cloud is located at ~ −3000 m (below sea level) in 2004 and at ~ −4000 m (below sea level) in 2014 (Figure 12a). Below Prati-9/Prati state 29, the bottom of the induced seismic cloud is located at ~−3200 m (below sea level) in 2008 and at ~−3700 m (below sea level) in 2014 (Figure 12b). Moreover, below Prati-32, the induced seismic cloud is located at ~−3400 m (below sea level) in 2011 and at ~−3600 m (below sea level) 2 years later (Figure 12c).

Consequently, in these three cases, where water was injected at different depths and different rates, the deepening of the microseismic events occurs at approximately the same rate of about 100 m/yr. This rate corresponds to the rate of rotation propagation of σ_1 below the injection well estimated during our simulation. Such an observation suggests that the rotation of the stress tensor deep below the injection well could favor the deepening of microseismicity and reactivation of preexisting fractures.

To investigate the effect of the stress tensor rotation on induced seismicity, we draw two Mohr's circle diagrams, with the assumption of a friction coefficient equal to 0.72 (Figure 13) to illustrate the mechanisms which could possibly happen at The Geysers. The first Mohr's circle diagram presents the state of stress before injection at ~500 m below the bottom of an injection well (here Prati-9 at $z = -2530$ m) (Figure 13a). In our simulation, at this depth the initial state of stress is $\sigma'_1 = Sv - P_f = \rho \times g \times z - P_f = (2700 \times 9.81 \times 2530) - 6.57 \times 10^6 = 60.4$ MPa, $\sigma'_2 = (0.95 \times \sigma_1) - P_f = 57.1$ MPa, and $\sigma'_3 = (0.34 \times \sigma_1) - P_f = 16.2$ MPa, with ρ the rock density, g the acceleration of gravity, z the depth, and P_f the fluid pressure. The blue point represents vertical

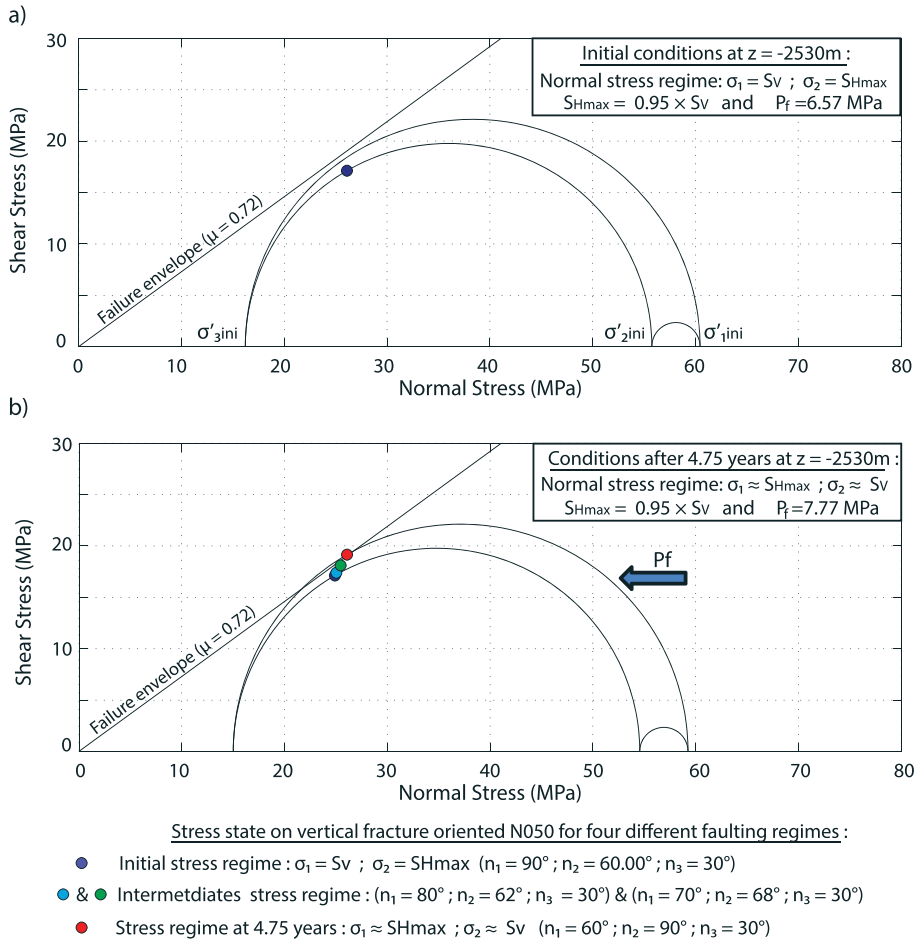

Figure 13. Schematic Mohr's circle diagrams showing the state of stress (a) before injection and (b) 4.75 years after the beginning of injection at ~500 m below the bottom of P-9. n_1, n_2, and n_3 are the angles between σ_1, σ_2, and σ_3 and the normal to the fracture plane.

fractures trending N50, which correspond to the fault plane family where most of the seismic events occur at reservoir depth at The Geysers [*Boyle and Zoback*, 2014]. We can see that these vertical fractures are not well oriented for a reactivation by the σ'_3/σ'_1 ratio but favorably oriented for a σ'_3/σ'_2 reactivation. In Figure 13b, we schematically represent how the pressure increase calculated after 4.75 years of injection leads to a decrease of the three effective principal stresses and shifts the Mohr's circle toward the failure envelope. We consider the rotation of the stress tensor by representing the normal and the shear stress acting on the vertical fractures N50 for four different state of stress: from normal faulting (blue point) to strike-slip faulting (red point). Two intermediate faulting regimes are also presented (cyan and green points). We observe that for the same effective stress, vertical fractures N50 will not be reactivated in a normal stress regime (blue point below the failure envelope) and reactivated in a strike-slip regime (red point above the failure envelope). This suggests that the rotation of the stress tensor below the injection wells can favor the reactivation of the preexisting fractures in locations where the increase in fluid pressure is too low to induce seismicity. This phenomenon can explain why the deepening of the microseismic events occurs at a rate of ~100 m/yr, which corresponds to the cooling-induced propagation rate for the rotation of σ_1 estimated during our simulation.

6. Conclusion

In this paper, we used the TOUGH-FLAC numerical simulator to investigate the spatiotemporal changes in the stress state within the northwest part of The Geysers geothermal field caused by injection of cold water. Good correlations were found between our results and previously published seismic focal plane mechanism

studies of Northwest Geysers stress changes. Our main finding is that changes in stress tensor orientation are caused by injection-induced progressive cooling of the reservoir, affected by seasonal variations in the injection rate. Because of gravity flow and cooling around a liquid zone formed by the injection, the vertical stress reduction is significant and propagates far below the injection well. At the same time, the horizontal stress increases, because of the stress redistribution associated with stress reduction inside the cooling area. These two phenomena cause the rotation of the stress tensor and the appearance of a strike-slip regime above, inside, and below the cooling area. This rotation favors the reactivation of the preexisting fractures deep below the injection wells and may therefore play a significant role in the observed long-term deepening of induced seismicity below an active injection well.

Acknowledgments

This work was conducted with funding provided by the Assistant Secretary for Energy Efficiency and Renewable Energy, Geothermal Technologies Program, under the U.S. Department of Energy contract DE-AC02-05CH11231. The seismic and injection data are available online at http://www.ncedc.org/egs/catalog-search.html and http://geosteam.conservation.ca.gov/WellSearch/GeoWellSearch.aspx, respectively.

References

Altmann, J. B., B. I. R. Müller, T. M. Müller, O. Heidbach, M. R. P. Tingay, and A. Weißhardt (2014), Pore pressure stress coupling in 3D and consequences for reservoir stress states and fault reactivation, *Geothermics*, doi:10.1016/j.geothermics.2014.01.004.

Aquaveo (2013), LLC in Provo, Utah. GMS User Manual (v9.0): The Groundwater Modeling System.

Boyle, K., and M. Zoback (2013), Stress and fracture orientation in the Northwest Geysers geothermal field, Proceedings of the 38th workshop on geothermal reservoir engineering, Stanford Univ., Stanford, Calif., 11–13 Feb.

Boyle, K., and M. Zoback (2014), The stress state of the Northwest Geysers, California geothermal field, and implications for fault-controlled fluid flow, *Bull. Seismol. Soc. Am.*, *104*(5).

Calpine Corporation (2012), NW Geysers Enhanced Geothermal System Demonstration Project, Update Report. [Available at http://www.geysers.com/docs/11022012%20EGS_Community%20Update%20Presentation.pdf.]

Davis, S. D., and C. Frohlich (1993), Did (or will) fluid injection cause earthquakes? Criteria for a rational assessment, *Seismol. Res. Lett.*, *64*, 207–224.

Garcia, J., C. Hartline, M. Walters, M. Wright, J. Rutqvist, P. F. Dobson, and P. Jeanne (2015), The Northwest Geysers EGS Demonstration Project, California—Part 1: Characterization and response to injection, *Geothermics*, doi:10.1016/j.geothermics.2015.08.003.

Häring, M. O., U. Schanz, F. Ladner, and B. C. Dyer (2008), Characterisation of the Basel 1 enhanced geothermal system, *Geothermics*, *37*, 469–495.

Hulen, J. B., B. A. Koenig, and D. L. Nielson (1995), The Geysers coring project, Sonoma County, California, USA - Summary and initial results, *Proc. World Geotherm. Congr.*, *2*, 1415–1420.

Hutchings, L., B. Bonner, A. Singh, S. Jarpe, and A. Singh (2014), Micro-earthquake analysis for reservoir properties at the Prati-32 injection test, The Geysers, California, Proceeding, Geothermal Resources Council, August.

Jaeger, J. C., N. G. W. Cook, and R. W. Zimmerman (2012), *Fundamentals of Rock Mechanics*, 4th ed., 475 pp., Wiley-India edition.

Jeanne, P., J. Rutqvist, C. Hartline, J. Garcia, P. F. Dobson, and M. Walters (2014a), Reservoir structure and properties from geomechanical modeling and microseismicity analyses associated with an Enhanced Geothermal System at The Geysers, California, *Geothermics*, *51*, 460–469.

Jeanne, P., J. Rutqvist, D. Vasco, J. Garcia, P. F. Dobson, M. Walters, C. Hartline, and A. Borgia (2014b), A 3D hydrogeological and geomechanical model of an Enhanced Geothermal System at The Geysers, California, *Geothermics*, *51*, 240–252.

Jeanne, P., J. Rutqvist, P. F. Dobson, J. Garcia, M. Walters, and C. Hartline (2014c), The impacts of mechanical stress transfers caused by hydromechanical and thermal processes on fault stability during hydraulic stimulation in a deep geothermal reservoir, *Int. J. Rock Mech. Min. Sci.*, *72*, 149–163.

Jeanne, P., J. Rutqvist, L. Hutchings, A. Singh, P. F. Dobson, M. Walters, C. Hartline, and J. Garcia (2015a), Degradation of the mechanical properties imaged by seismic tomography during an EGS creation at The Geysers (California) and geomechanical modeling, *Phys. Earth Planet. In.*, *240*, 82–94.

Jeanne, P., J. Rutqvist, A. P. Rinaldi, P. F. Dobson, M. Walters, C. Hartline, and J. Garcia (2015b), Seismic and aseismic deformations and impact on reservoir permeability: The case of EGS stimulation at The Geysers, California, USA, *J. Geophys. Res. Solid Earth*, *120*, doi:10.1002/2015JB012142.

Lipman, S. C., C. J. Strobel, and M. S. Gulati (1978), Reservoir performance of The Geysers field, *Geothermics*, *7*, 209–219.

Lockner, D. A., R. Summer, D. Moore, and J. D. Byerlee (1982), Laboratory measurements of reservoir rock from the Geysers Geothermal Field, California, *Int. J. Rock Mech. Min. Sci.*, *19*, 65–80.

Martínez-Garzón, P., M. Bohnhoff, G. Kwiatek, and G. Dresen (2013), Stress tensor changes related to fluid injection at The Geysers geothermal field, California, *Geophys. Res. Lett.*, *40*, 2596–2691, doi:10.1002/grl.50438.

Martínez-Garzón, P., G. Kwiatek, H. Sone, M. Bohnhoff, G. Dresen, and C. Hartline (2014), Spatiotemporal changes, faulting regimes, and source parameters of induced seismicity: A case study from The Geysers geothermal field, *J. Geophys. Res. Solid Earth*, *119*, 8378–8396, doi:10.1002/2014JB011385.

Oppenheimer, D. C. (1986), Extensional tectonics at the Geysers Geothermal Area, California, *J. Geophys. Res.*, *91*, 11,463–11,476, doi:10.1029/JB091iB11p11463.

Rutqvist, J. (2011), Status of the TOUGH-FLAC simulator and recent applications related to coupled fluid flow and crustal deformations, *Comput. Geosci.*, *37*, 739–750.

Rutqvist, J., and C. Oldenburg (2007), Analysis of cause and mechanism for injection-induced seismicity at the Geysers geothermal field, *Geotherm. Resour. Counc. Trans.*, *31*, 441–445.

Rutqvist, J., and C. M. Oldenburg (2008), Analysis of injection-induced micro-earthquakes in a geothermal steam reservoir, Geysers Geothermal Field, California, Proceedings of the 42th U.S. Rock Mechanics Symposium, Paper 151, San Francisco, Calif., 29-2 July.

Rutqvist, J., Y.-S. Wu, C.-F. Tsang, and G. Bodvarsson (2002), A modeling approach for analysis of coupled multiphase fluid flow, heat transfer, and deformation in fractured porous rock, *Int. J. Rock Mech. Min. Sci.*, *39*, 429–442.

Rutqvist, J., P. F. Dobson, J. Garcia, C. Hartline, P. Jeanne, C. M. Oldenburg, D. W. Vasco, and M. Walters (2015a), The Northwest Geysers EGS Demonstration Project, California: Pre-stimulation modeling and interpretation of the stimulation, *Math. Geosci.*, *47*, 3–26.

Rutqvist, J., P. Jeanne, P. F. Dobson, J. Garcia, C. Hartline, L. Hutchings, A. Singh, D. W. Vasco, and M. Walters (2015b), The Northwest Geysers EGS Demonstrations Project, California—Part 2: Modeling and interpretation, *Geothermics*, doi:10.1016/j.geothermics.2015.08.002.

Schoenball, M., L. Dorbath, E. Gaucher, J. Florian Wellmann, and T. Kohl (2014), Change of stress regime during geothermal reservoir stimulation, *Geophys. Res. Lett.*, *41*, 1163–1170, doi:10.1002/2013GL058514.

Segall, P., and S. D. Fitzgerald (1998), A note on induced stress changes in hydrocarbon and geothermal reservoirs, *Tectonophysics*, *289*, 117–128.

Williams, C., S. P. Glanis, T. H. Moses, and F. V. Grubb (1993), Heat flow studies in the Northwest Geysers geothermal field, CA, *GRC Trans.*, *17*, 281–288.